



23 volatile-saturated conditions and in the presence of F-rich fluid with numerous thorite  
24 and xenotime inclusions, have intermediate lattice parameters ( $a=6.649\text{\AA}$ ,  $c=6.020\text{\AA}$ ).  
25 Pyramidal zircon grains (Type-2), formed in a subsolvus granite system at relatively  
26 low temperatures and coexisted with fluid inclusions, have the biggest lattice  
27 parameters ( $a=6.677\text{\AA}$ ,  $c=6.010\text{\AA}$ ). Trace element, including Hf, Th, Ti, Y and REE,  
28 and volatiles contents increase in the structure of zircons from the early- to  
29 late-magmatic origin, which is consistent with the expansion of the lattice parameters.  
30 The occurrence of the three zircon types in the Xiangshan arfvedsonite granites is  
31 interpreted to reflect the progressive fractionation of granitic melt from hypersolvus to  
32 subsolvus conditions. Therefore, we conclude that the lattice expansion of zircon in  
33 this study results from chemical incorporation of trace element and volatile  
34 components during the magmatic to hydrothermal evolution of granitic magma.  
35 Besides, the textural and compositional evolution of zircon can be used as efficient  
36 indices for the fractionation and evolution of A-type granitic system.

37 **Keywords:** Chemical lattice expansion, zircon, fractionation crystallization,  
38 magmatic-hydrothermal evolution, A-type granite

39

## 40 INTRODUCTION

41 Zircon is a common accessory mineral in granitic rocks. It is chemically resistant,  
42 relatively insoluble and refractory, and can withstand weathering and recycling, as  
43 well as high temperature metamorphism and anataxis (El-Bialy and Ali 2013). It is  
44 widely accepted that zircon can provide reliable and robust estimates of age,

45 compositions of coexisting minerals and melts, and constraints on the petrogenesis of  
46 host rocks (Valley 2003). In spite of its apparently simple chemical composition  
47 ( $\text{ZrSiO}_4$ ), zircon is able to accept substantial amounts of other minor and trace  
48 elements into its crystal lattice (e.g., Hf, Th, U, Ti, Nb, Ta, P, Y and REE) (Breiter et  
49 al. 2014). Zircon crystals that are not affected by intense metamictization could  
50 provide information about the chemical composition of the melt from which they  
51 crystallized. In contrast, the metamict crystals may accumulate substantial amounts of  
52 non-formula elements, re-equilibrated with the hydrothermal and low-temperature  
53 fluids (Geisler et al. 2007; Yang et al. 2014).

54 In granitic systems, zircon is generally considered to form early in the  
55 crystallization history (Valley 2003). However, in some A-type granites it can  
56 crystallize during the whole process of magmatic crystallization, with significant  
57 distinction in both texture and composition (Belousova et al. 2006; Breiter and Škoda  
58 2012; Pupin 1980). Although geologically complicated, the behavior of trace elements  
59 in zircon depends on physical-chemical conditions and partition coefficients between  
60 zircon and melt (Belousova et al. 2006). Presently, there are several speculations have  
61 been proposed regarding zircon texture and composition, which include that zircon  
62 can record the processes of (1) magmatic and hydrothermal crystallization (Van  
63 Lichtervelde et al. 2009; Yang et al. 2013), (2) hydrothermal alteration (Zheng et al.  
64 2007), (3) country-rock assimilation, (4) magma mixing (Griffin et al. 2002), or even  
65 (5) tectonic setting (Grimes et al. 2007, 2009).

66 This study reports analyses of textures and compositions of three types of zircon

67 from an A-type granite in north China. The purposes of this article are (1) to  
68 determine the variation of zircon in both structure and composition that may influence  
69 the lattice expansion, and (2) to test the speculation that zircon could record the  
70 processes of magmatic and hydrothermal evolution of the host granite. All samples  
71 come from the Xiangshan arfvedsonite-bearing granite. Zircon structures were  
72 analyzed by X-ray diffraction (XRD), cathodoluminescence (CL) and Raman  
73 spectroscopy. Major and trace element compositions of zircon were measured by  
74 EMPA and LA-ICPMS.

## 75 **GEOLOGICAL BACKGROUND**

76 The Xiangshan complex crops out over 217 km<sup>2</sup> in the NNE-trending Yanshan  
77 Mountains (northeastern Hebei province), on the northern margin of the North China  
78 Craton (NCC) (Fig. 1a). It intruded into the Lower Sinian migmatite, with limestones  
79 of the Cambrian Fushanjuan Formation and the Jurassic Mentougou Formation in the  
80 northeast. It consists of medium-grained arfvedsonite granite in the center and  
81 porphyritic biotite granite on the margins (Fig.1b). The arfvedsonite granites mainly  
82 consist of quartz (25–30 vol%), perthite (45–55 vol%), K-feldspar (10–15 vol%),  
83 plagioclase (5 vol%) and minor arfvedsonite (5 vol%). Accessory minerals mainly  
84 consist of zircon, magnetite, sphene, fluorite and rutile. The quartz is subhedral to  
85 euhedral and 1–3 mm in size. The perthite is commonly subhedral and 1–4 mm in size,  
86 with perthitic texture. The K-feldspar is also commonly subhedral and 2–4 mm in size.  
87 The arfvedsonite is blue to dark blue in color, euhedral to subhedral with distinct  
88 pleochroism. Some arfvedsonite grains occur as inclusions within quartz or perthite,



110 expose the internal structures. The crystals were documented with transmitted and  
111 reflected light micrographs as well as by CL images to reveal their external and  
112 internal textures.

113 Single crystal micro-XRD analyses were conducted using a Rigaku D/max Raxis  
114 IIR micro-XRD system at the Central South University, Changsha, China. All  
115 analyses were carried out with a beam diameter of ~100  $\mu\text{m}$  under 40 kV and 250 mA  
116 ( $\text{CuK}\alpha$ ) with exposures of 20 minutes.

117 Laser Raman spectra of zircon crystals were collected using the HORIBA XploRA  
118 Plus Laser Raman micro-spectroscopy at the Key Laboratory of Mineralogy and  
119 Metallogeny, Chinese Academy of Sciences (CAS), Guangzhou, China. An Ar ion  
120 laser, operating at 10mW was used to produce the excitation wavelength of 532 nm.  
121 The beam was coupled with a grating of 1200 grooves per mm. The scanning range of  
122 the spectra was set between 100 and 1500  $\text{cm}^{-1}$  with an accumulation time of 8 s for  
123 each scan.

124 Major element compositions of zircon grains and host inclusions were analyzed  
125 using a JEOL JXA 8230 electron microprobe (EMPA) at the Key Laboratory of  
126 Mineralogy and Metallogeny, Guangzhou Institute of Geochemistry, CAS,  
127 Guangzhou, China. The operating conditions were as follows: 15 kV accelerating  
128 voltage, 20 nA beam current and 1  $\mu\text{m}$  beam diameter. Zr and Si were analyzed for  
129 20s on peak and 10s on background whereas Fe, P, Ti, U, Y, Hf and Th were analyzed  
130 for 40s on peak and 20s on background. Standards used for analyses of the zircon

131 samples include zircon for Zr, Si, and Hf, magnetite for Fe, rutile for Ti, monazite for  
132 U, Y and Th and apatite for P. ZAF calibration procedures were used for data  
133 correction.

134 Trace element analyses of the zircon grains was conducted with an Agilent 7500a  
135 ICP-MS coupled with a Resonetics RESolution M-50 193nm laser-ablation system at  
136 Key Laboratory of Mineralogy and Metallogeny, CAS. More detailed analytical  
137 procedures were described by Li et al. (2012) and Tu et al. (2011). All analyses were  
138 carried out with a beam diameter of 31  $\mu\text{m}$  and a repetition rate of 10Hz with an  
139 energy of 80mJ. Helium was used as the carrier gas. NIST SRM610 and TEMORA2  
140 (TEM) were used as external standards (Black et al. 2004; Pearce et al. 1997), and  
141  $^{29}\text{Si}$  as an internal standard (Anczkiewicz et al. 2001). All analysis spots were  
142 carefully selected to avoid mineral and melt inclusions and cracks in zircons. Only  
143 smooth LA-ICPMS signals were chosen.

## 144 RESULTS

### 145 Zircon morphology and textures

146 Zircons in the Xiangshan arfvedsonite granites can be morphologically classified  
147 into prismatic (Type-1) and pyramidal (Type-2) types. Moreover, the prismatic zircon  
148 grains can be further subdivided into two subtypes, bright and zoned zircon (Type-1A)  
149 and murky and spongy zircon (Type-1B), according to their internal structures.

150 Type-1A zircons commonly intergrowth with quartz, K-feldspar and arfvedsonite,  
151 or enclosed in arfvedsonite (Fig. 3a). They are euhedral prismatic crystals 80–120  $\mu\text{m}$

152 in length with  $c/a$  ratios of 2:1 to 3:1. They are transparent in transmitted light, display  
153 multiple oscillatory growth zones in CL images but are homogeneous under BSE,  
154 consistent with zircon of magmatic origin (Fig. 3d). They have well-developed  $\{101\}$   
155 pyramids and  $\{100\}$  and  $\{110\}$  prisms, similar to typical morphologies of high  
156 temperature zircon in alkaline magma (Pupin 1980). Inclusions in the zircon grains  
157 commonly consist of melt and/or crystallized minerals such as apatite (Fig. 3g).

158 Type-1B zircons are usually intergrowth with quartz, K-feldspar and arfvedsonite  
159 (Fig. 3b), or enclosed in quartz and K-feldspar, with apparent radiohalo. These zircon  
160 crystals are euhedral prismatic crystals 100–200  $\mu\text{m}$  in length with  $c/a$  ratios of 2:1 to  
161 3:1. They are cloudy and redbrown in transmitted light, with no oscillatory growth  
162 zones in CL images (Fig. 3e). They have well-developed  $\{101\}$  pyramids and  $\{100\}$   
163 and/or  $\{110\}$  prisms, similar to the typical morphologies of high temperature zircons  
164 (Pupin, 1980). Inclusions in the zircons crystals commonly consist of melt and/or  
165 crystallized minerals such as apatite, thorite, Fe-oxide and xenotime (Fig. 3h).  
166 Sometimes, the murky Type-1B zircon can also be found as overgrowths of Type-1A  
167 zircon crystals (Figs. 4a and 4b).

168 Type-2 zircons are usually enclosed in quartz, K-feldspar or graphic textured  
169 occurrences of the two (Fig. 3c). Halite-bearing fluid inclusions can be observed in  
170 the host quartz coexist with the Type-2 zircon (Fig. 3i). The Type-2 zircon grains are  
171 dipyramidal with lengths of 100–280  $\mu\text{m}$ . They are cloudy and red-brown in  
172 transmitted light, and have a transparency between Type-1A and Type-1B zircons.  
173 They display slight oscillatory growth zones in CL images (Fig. 3f) with rare



174 inclusions. They have well-developed {111} crystal faces with sporadically  
175 less-developed {110} faces.

## 176 **XRD patterns**

177 The XRD pattern of Type-1A zircon crystals have cell parameters of  $a=6.603(2)$   
178 Å and  $c=5.971(4)$  Å identical to the standard zircon (06-0266,  $a=6.607$  Å,  $c=5.982$  Å)  
179 (Table 1) (Robinson et al. 1971). The strong intensity, small cell parameters, along  
180 with the sharp two-theta of {220} peak of full-widths at half-maximum (FWHM) of  
181  $0.174^\circ$  (Fig. 5), indicating that they are well-crystallized and of magmatic origin  
182 (Crepaldi et al. 2003). The cell parameters of the Type-1B zircon are  $a=6.649(6)$  Å and  
183  $c=6.020(2)$  Å which are higher than both the Type-1A zircon and the standard zircon.  
184 The shifting of {220} peak position to slightly lower two-theta and a remarkable  
185 reduction in intensity and broadening of the peak (FWHM= $0.635^\circ$ ) suggest that the  
186 Type-1B zircon grains have low crystallinity (Fig. 5). The cell parameters of the  
187 Type-2 zircon are  $a=6.677(7)$  Å and  $c=6.010(4)$  Å. The {220} peak position shifts to  
188 lower two-theta than the other two types of zircon with low peak intensities between  
189 the other two types of zircon. The FWHM of the Type-2 zircon is  $0.172^\circ$  which is  
190 similar to that of the Type-1A zircon (Fig. 5).

## 191 **Zircon compositions**

192 Major and trace element compositions of the zircons are listed in Supplemental  
193 Data Table 2 and Supplemental Data Table 3, respectively. Type-1A zircons have 31.6–  
194 33.0 wt% SiO<sub>2</sub>, 63.2–65.7 wt% ZrO<sub>2</sub>, 1.06–1.82 wt% HfO<sub>2</sub> and 0.03–1.42 wt% Y<sub>2</sub>O<sub>3</sub>

195 (mostly in the range of 0.03–1.00 wt%). Total REE contents vary from 855 to 2902  
196 ppm with LREE/HREE ratios of 0.03 to 0.05. They display positive Ce anomalies and  
197 negative Eu anomalies with Ce/Ce\* and Eu/Eu\* ratios ranging from 9.50–53.7 and  
198 0.008–0.05, respectively (Fig. 6a). They have La and Pr concentrations ranging from  
199 0.08 to 3.15 ppm, 0.12 to 1.05 ppm, respectively. Type-1A zircons have relatively low  
200 contents of Y (1274–4652 ppm), Th (51.6–465 ppm) and U (96.6–693 ppm), with  
201 Th/U ratios ranging from 0.39–0.67 (Fig. 6b).

202 Type-1B zircons have 30.8–32.6 wt% SiO<sub>2</sub>, 59.5–65.9 wt% ZrO<sub>2</sub>, 1.29–4.34 wt%  
203 HfO<sub>2</sub> and 0.05–2.36 wt% Y<sub>2</sub>O<sub>3</sub> (mostly in the range of 1.00–2.36 wt%). Total REE  
204 contents vary from 4,240 to 16,057 ppm with LREE/HREE ratios of 0.03 to 0.11.  
205 They display positive Ce anomalies and negative Eu anomalies with Ce/Ce\* and  
206 Eu/Eu\* ratios ranging from 1.31–43.0 and 0.009–0.07, respectively (Fig. 6a).  
207 Compared to Type-1A zircons, Type-1B zircons have much higher contents of Y  
208 (5178–27020 ppm), Th (2308–27524 ppm) and U (3099–11450 ppm) (Figs. 4d–e),  
209 with Th/U ratios ranging from 0.59–2.42. Notably, they also have much higher La, Pr,  
210 Hf, Y, P, Nb and Ta concentrations than the Type-1A zircons (Figs. 4f–h and 6b).

211 Type-2 zircons have 30.2–32.3 wt% SiO<sub>2</sub>, 53.3–61.4 wt% ZrO<sub>2</sub>, 1.33–3.08 wt%  
212 HfO<sub>2</sub> and 1.07–6.29 wt% Y<sub>2</sub>O<sub>3</sub>. They have the highest total REE contents varying  
213 from 14952 to 24139 ppm with LREE/HREE ratios of 0.05 to 0.11. They display  
214 obviously positive Ce anomalies and negative Eu anomalies with Ce/Ce\* and Eu/Eu\*  
215 ratios ranging from 24.0–117 and 0.007–0.01, respectively (Fig. 6a). They have La, Pr  
216 concentrations ranging from 0.45 to 3.25 ppm, 8.01 to 17.3 ppm, respectively.

217 Compared to Type-1A and Type-1B zircons, Type-2 zircons have relatively high  
218 contents of Y (27347–42189 ppm), Th (3935–17265 ppm) but moderate U (616–4982  
219 ppm) contents, with highest Th/U ratios ranging from 2.46–12.9. They also have  
220 much higher Hf, Y, P, Nb, Ta contents than Type-1A zircon grains (Fig. 6b).

## 221 **DISCUSSION**

### 222 **Origin of the three types of zircon**

223 The different morphology, texture and composition of the three zircon types in the  
224 Xiangshan arfvedsonite granites is interpreted to indicate that they formed under  
225 different physical and chemical conditions during the magmatic-hydrothermal  
226 evolution of the intrusion. In typical I- and S-type granites, zircon is one of the first  
227 crystallizing minerals (Belousova et al. 2006; Breiter and Škoda 2012), however, in  
228 some A-type granites it can crystallize throughout the fractionation process (Breiter  
229 and Škoda 2012), consistent with what is seen in the zircons from the Xiangshan  
230 arfvedsonite granites. The texture and composition of zircon can reflect the evolution  
231 process of magma and provide information to the role played by volatiles (Erdmann et  
232 al. 2013).

233 Type-1A zircons show magmatic textural and compositional features (Pupin 1980)  
234 particularly the oscillatory zoning. In addition, the well-developed {101} pyramids  
235 and {100} prisms, as well as the occurrence of melt and apatite inclusions, indicate  
236 that they crystallized from high temperature alkaline magma (Pupin 1980).  
237 Furthermore, the low Th, U and Hf concentrations and high  $ZrO_2/HfO_2$  ratios (Figs.

238 7a–c) indicate they crystallized from a volatile-undersaturated magma (Erdmann et al.  
239 2013). Therefore, the Type-1A zircons are most likely primary magmatic zircon that  
240 crystallized early in the evolution of the granitic magma.

241 The presence of Type-1B zircon overgrowths on some Type 1A zircons indicates  
242 they crystallized later in the evolution of the magma (Figs. 5a–b). They have higher  
243 FWHMs of Raman and XRD than Type-1A zircon crystals (Figs. 5c and 6), indicating  
244 lower crystallinities. The Type-1B zircons show altered textures and exotic  
245 composition and well-developed {101} pyramids and {100} prisms, but larger grain  
246 size, higher Th, U and HfO<sub>2</sub> concentrations, lower ZrO<sub>2</sub>/HfO<sub>2</sub> (Figs. 7a–c), and no  
247 oscillatory growth zones compared to Type-1A. The porous and altered features are  
248 similar to those of the zircon from evolved granite plutons at Melville Peninsula in  
249 northern Canada which were interpreted to be from volatile-saturated magmas  
250 (Erdmann et al. 2013). In addition, thorite and xenotime, which commonly form at the  
251 late stage of the magmatic evolution, can be observed as inclusions in the Type-1B  
252 zircons. Combined these features suggests that the Type-1B zircons crystallized from  
253 a relatively evolved magma and were subsequently altered in a volatile-saturated  
254 magma.

255 The Type-2 zircons show morphology characteristic of low-temperature and  
256 fluid-rich magmas (Pupin 1980). The well-developed {111} crystal faces with  
257 sporadically less-developed {110} faces are similar to synthetic, flux-grown zircon  
258 crystals (Burakov et al. 2002). In addition, some Type-2 zircon crystals are  
259 intergrowth with quartz and K-feldspar, which would have formed under subsolvus

260 condition. Formation of myrmekitic texture involve a series of short pluses of  
261 infiltration of an aqueous fluid at about 500 °C during the subsolvus evolution of the  
262 granite (Abart et al. 2014). The coexistence of halite-bearing fluid inclusions with  
263 Type-2 zircon crystals is consistent with a late magmatic or hydrothermal origin  
264 (Schaltegger 2007). So we suggest that the Type-2 zircons formed under subsolvus  
265 conditions with volatile over-saturated.

### 266 **Lattice expansion of zircon induced by chemical incorporation**

267 Standard zircon has tetragonal symmetry with  $a=6.607 \text{ \AA}$ ,  $c=5.982 \text{ \AA}$ ,  $Z=4$  and  
268 belongs to the space group  $I4_1/amd$  (Robinson et al. 1971). Such crystal structure is  
269 documented that can be expanded by thermal heating, metamictization and chemical  
270 incorporation (Robinson et al. 1971; Patwe et al. 2009). In this study, natural zircon  
271 lattice show expansion from the early- to late-stage zircon types that formed during  
272 the cooling and fractionation of the Xiangshan granitic magma, instead of thermal  
273 heating. Meanwhile, the XRD and Raman data also lend little support for remarkable  
274 influence of metamictization. The altered Type-1B zircon shows the most metamict  
275 features among the three zircon types, but the crystallographic parameters is not the  
276 biggest type (Fig. 5). Therefore, chemical incorporation in zircon lattice should be the  
277 mostly plausible cause. Since chemical compositions of zircon from igneous rocks are  
278 controlled by the behavior of trace element and partition coefficient between zircon  
279 and melt (Belousova et al. 2006), the remarkable increasing of trace element  
280 substitution and volatile contents in zircon lattice of this study depend on  
281 physical-chemical conditions of the evolving granitic system.

282 **Substitution increases from early to late zircon lattice.**

283 In granitic rocks, non-formula elements, such as Hf, Th, U, REE and Y can enter  
284 into the zircon lattice by simple or coupled substitution mechanisms (Hanchar et al.  
285 2001; Hoskin and Schaltegger 2003). IV charge (+4) cations, such as  $\text{Hf}^{4+}$ ,  $\text{Th}^{4+}$ ,  $\text{U}^{4+}$   
286 and  $\text{Ti}^{4+}$ , can substitute for  $\text{Zr}^{4+}$ , whereas other charge cations, such as  $\text{Y}^{3+}$ ,  $\text{REE}^{3+}$ ,  
287  $\text{Nb}^{5+}$ ,  $\text{Ta}^{5+}$ ,  $\text{P}^{5+}$  and  $\text{Fe}^{2+}$ , can undergo coupled substitution for  $\text{Zr}^{4+}$  and  $\text{Si}^{4+}$ . In this  
288 study, the substitution contents of such non-formula elements are much more favored  
289 in the late-stage zircon formed during the magmatic-hydrothermal evolution of  
290 alkaline granite (Table 2).

291 IV charge non-formula cations usually occur as major element in zircon. For  
292 example,  $\text{Hf}^{4+}$  and  $\text{Zr}^{4+}$  have identical charge (+4) and similar cation radius (0.83 Å  
293 for  $\text{Hf}^{4+}$  and 0.84 Å for  $\text{Zr}^{4+}$ ), so they can substitute for each other and form complete  
294 zircon-hafnon solid solution series. It was confirmed by the study of Wang et al.  
295 (1996), who found an extreme Hf enrichment (up to 34.8 wt%  $\text{HfO}_2$ ) in zircon from  
296 an A-type granite in Suzhou, China. Besides,  $\text{Th}^{4+}$  and  $\text{U}^{4+}$  have the same charge (IV)  
297 but larger cation radius (1.05 Å for  $\text{U}^{4+}$  and 1.00 Å for  $\text{Th}^{4+}$ ), and can also substitute  
298  $\text{Zr}^{4+}$  in zircon (Hoskin and Hanchar 2003). For example, the Th and U contents in  
299 zircons from the A-type granite in the Pitinga tin deposit, Brazil, can reach 6000 ppm  
300 and 2900 ppm, respectively, and the  $\text{ThO}_2$  and  $\text{UO}_2$  contents in zircons from the  
301 Beauvoir S-type granite, France can reach 0.35 wt% and 7.6 wt%, respectively  
302 (Cheng et al. 1992). In this study, the altered magmatic zircon (Type-1B) and late  
303 zircon (Type-2) from the Xiangshan arfvedsonite granite have significantly higher

304 contents of Hf, U and Th than the early zircon (Type-1A) (Figs. 7a–c), indicating that  
305 Hf, U and Th can be concentrated in both residual melt and late zircon during the  
306 fractional crystallization. It is consistent with the well-documented zircon–hafnon  
307 solid solution that natural zircon may contain high contents of Hf, and changes into  
308 hafnian zircon or even hafnon in some high fractionated granite systems (Wang et al.  
309 1996; Yin et al. 2013). The isomorphous substitutions of  $\text{Th}^{4+}$  and  $\text{U}^{4+}$  for  $\text{Zr}^{4+}$  lead to  
310 the expansion of unit-cell, which is reflected in the low-degree shift of XRD peaks of  
311 the Type-1B and Type-2 zircons (Fig. 5). The extensive substitutions of  $\text{Th}^{4+}$  and  $\text{U}^{4+}$   
312 resulted in the metamictization of the Type-1B zircon which reacted with magmatic  
313 exsolved fluids. It seems likely that the substitution of IV charge cation in zircon  
314 lattice can become easier in the late magmatic stage.

315       Alternatively, the other charge cations,  $\text{REE}^{3+}$  and  $\text{Y}^{3+}$  in particular, usually occur  
316 as incompatible trace elements in zircon. REE-bearing zircon commonly contains P,  
317 and owing to crystal chemical resemblance between  $\text{Y}^{3+}$  and heavy  $\text{REE}^{3+}$ ,  
318 substitution of  $\text{Zr}^{4+}$  by  $\text{REE}^{3+}$  or  $\text{Y}^{3+}$  and  $\text{Si}^{4+}$  by  $\text{P}^{5+}$  in zircon is commonly explained  
319 by the coupled xenotime-type substitution to maintain charge balance  
320  $[(\text{Y,REEs})^{3+} + \text{P}^{5+} \rightarrow \text{Zr}^{4+} + \text{Si}^{4+}]$ . If xenotime substitution is the sole mechanism by which  
321 charge balance is maintained in zircon crystals that have undergone REE-substitution  
322 (Hoskin 2003), the atomic ratio  $(\text{REE} + \text{Y})/\text{P}$  should approach 1. As the majority of  
323  $(\text{REE} + \text{Y})/\text{P}$  ratios in zircons from the Xiangshan arfvedsonite granites are higher than  
324 1 (Fig. 7d), this suggests a more complex charge-balance mechanism (Cavosie et al.  
325 2006; Finch and Hanchar 2003). Because the Type-1B and Type-2 zircons have

326 relatively high Nb and Ta contents and low total weight of EMPA data, the  
327 substitution  $(Y, REEs)^{3+} + (Nb, Ta)^{5+} \rightarrow 2Zr^{4+}$  and  $(ZrO)^{2+} \rightarrow (YOH)^{2+}$  or  $(ZrO)^{2+} \rightarrow (YF)^{2+}$   
328 proposed by Es'kova (1959) may also play a role. Nevertheless, the obvious increase  
329 of REE and Y concentrations from the early to late zircon structure suggests that the  
330 coupled substitution in the zircon lattice increases from early to late magmatic stage.

### 331 **Volatile becomes saturated.**

332 The deficit in the total weight of EMPA is commonly ascribed to the presence of  
333 the  $OH^-$  and  $F^-$  in the zircon's structure or molecular  $H_2O$  in the amorphous domains  
334 of the metamict zircon structure (Breiter and Škoda 2012). Previous authors predicted  
335 that hydration takes place only in tetrahedral sites ( $SiO_4$ ) without affecting the  
336 occupancy of the Zr position (Hoskin 2003). For example, up to 8.8 wt%  $H_2O$  was  
337 found in Archaean zircon from Jack Hills, Australia (Nasdala et al. 2009), and as  
338 much as 0.8 apfu  $(OH, F)_4$  replacing the  $(SiO_4)$  group was found in synthesized zircon  
339 (Caruba et al. 1985). In this study, the deficits of the  $SiO_2$  contents (32.8- $SiO_2$  wt%)  
340 of Type-1B (0.2–2.0 wt%) and Type-2 (0.5–2.6 wt%), which are much higher than  
341 that of Type-1A zircon (0–1.2 wt%), are indicative of their increasing of volatiles  
342 substitution. Giving that the F and Cl contents nearly below detection limit  
343 (Supplemental Data Tble2), the dominate volatile is probably  $H_2O$  or  $OH^-$  in the three  
344 types of zircon. Meanwhile, the significant deficits of the total weight (1-Total) of  
345 Type-1B (1.1–5.3 wt%) and Type-2 (1.6–6.7 wt%) are indicative of their increasing  
346 of trace elements as well as volatiles (Fig. 8).

347 The logarithms of REE partition coefficients between mineral and melt against



348 ionic radii show a simple parabolic relationship (Onuma et al. 1968), which is  
349 consistent with the crystal structural strain modelling (Blundy and Wood 1994). Most  
350 REEs of Type-1A and Type-2 zircon grains fall on the parabola, except for Ce and Eu  
351 (Figs. 9a and 9c), which are largely affected by their valences. On the contrary, the  
352 Type-1B zircon grains have more elements (e.g., Ce, Eu, La, Pr and Nd) deviating  
353 from the predicted parabolic behavior (Fig. 9b), suggesting hydrothermal alteration  
354 plays an essential role in the enrichment of La, Pr and Nd. Such  
355 non-charge-and-radius-controlled behaviors of REE distribution has been attributed to  
356 the transition between pure silicate melts and hydrothermal fluids by Bau (1996). The  
357 trace element behaviors, therefore, also support that the Type-1B and Type-2 zircons  
358 were formed in subsolvus granitic melt with volatile-saturated at the late magmatic  
359 stage.

## 360 **IMPLICATIONS**

361 Accordingly, magmatic-hydrothermal evolution of granitic magma usually comes  
362 along with fractional crystallization and fluid exsolution, which could be recorded in  
363 zircon (Fig. 10). The formation of the altered zircon crystals (Type-1B) suggests that  
364 they formed during the magmatic-hydrothermal transition stage in the evolution of  
365 granitic magma. Such transitional stages are characterized by the coexistence of melt,  
366 crystal, and fluid phases (Burnham 1979). The incompatible elements (including  
367 HFSEs and volatiles) would concentrate in the alkaline and fluid-rich residual melt,  
368 from which subsolvus granite later crystallized. Exsolved magmatic fluids and other  
369 volatiles that are enriched in HFSEs and F could alter the previous minerals, including

370 zircon. Meanwhile, metamictization caused by self-irradiation would generate  
371 structural damage that would facilitate fluid-mineral interaction during the  
372 magmatic-hydrothermal transition. Therefore, the enhancing substitution of trace  
373 elements and volatile component in zircons could undoubtedly result in chemical  
374 lattice expansion, during the magmatic-hydrothermal evolution of granitic magma.

375       This study also shows that magmatic-hydrothermal evolution can be an efficient  
376 way to mobilize Zr from the magmatic to the hydrothermal system, even in ore-barren  
377 alkaline granite. Because HFSEs have high charge-to-ionic-radius ratios, they are  
378 generally incompatible during magmatic fractionation (Finlow-Bates and Stumpfl,  
379 1981). There is increasing evidence that these elements are mobile in some cases and  
380 can be concentrated as a result of high degrees of fractional crystallization from  
381 evolved granitic and pegmatitic melts, especially in rare-metal mineralized  
382 alkaline-peralkaline system (Aja et al. 1995; Ayers et al. 2012; Bau and Dulski 1995;  
383 Rubin et al. 1993; Veksler et al. 2005). For example, the hypersolvus granite of the  
384 Strange Lake complex contains ca. 3000 ppm Zr on average, and ca. 500 ppm REE  
385 and Y, whereas the subsolvus granite has 3.25 wt% ZrO<sub>2</sub>, 0.66 wt% Y<sub>2</sub>O<sub>3</sub> and 1.30 wt%  
386 REE oxides (Salvi and Williams-Jones 2006), indicating highly remobilization of Zr,  
387 REE, and Y during magmatic-hydrothermal evolution. Similar cases are also reported  
388 in peralkaline granites from the Amis complex in Namibia (Schmitt et al. 2002) and  
389 from the Khadlzan-Buregtey in Mongolia (Kovalenko et al. 1995). In the Baerzhe  
390 pluton, the contents of ZrO<sub>2</sub> increases from < 0.5 wt% in the hypersolvus granite to 3  
391 wt% in the subsolvus granite, and Nb<sub>2</sub>O<sub>5</sub> from < 0.02 to 0.28 wt% and Ce<sub>2</sub>O<sub>3</sub> from <

392 0.1 to 0.4 wt%, indicating that Zr, REE, and Nb are mainly precipitated in the  
393 late-stage subsolvus melt that was rich in H<sub>2</sub>O, alkalis, and F (Yang et al. 2014).  
394 Mobility of HFSEs is also documented in ore-barren alkaline granitic system. For  
395 example, hafnium was documented sharply increase within zircon from the late-facies  
396 of the Suzhou granite (Wang et al. 1996). Similarly, high concentration of Th in zircon,  
397 from peralkaline granite in Eastern China, was also mobilized as thorite inclusion by  
398 hydrothermal alteration (Xie et al. 2005). In this study of the Xiangshan alkaline  
399 granite, the textures and compositions of the altered and late magmatic zircon types  
400 indicate that the mobility of Zr, Hf, U, Th, Y and REE, as well as volatiles, and can  
401 also be efficient during the magmatic-hydrothermal evolution of ore-barren alkaline  
402 A-type granites.

403

404

#### ACKNOWLEDGMENTS

405 This study was financially supported by the National Nature Science Foundation  
406 of China grants (41472062 and 41373031). We sincerely thank the Dr. Li Cong-Ying,  
407 Dr. Tan Da-Yong, Dr. Tu Xiang-Lin, and Mrs. Hu Guang-Qian of the CAS Key  
408 Laboratory of Mineralogy and Metallogeny at GIGCAS for their substantial  
409 assistance during the laboratory works. We also thank the two anonymous reviewers  
410 for constructive comments and Pete Hollings for polish English.

411

412

#### REFERENCES CITED

413 Abart, R., Heuser, D., and Habler, G. (2014) Mechanisms of myrmekite formation:

- 414 case study from the Weinsberg granite, Moldanubian zone, Upper Austria.  
415 Contributions to Mineralogy and Petrology, 168, 1–15.
- 416 Aja, S.U., Wood, S.A., and Williams-Jones, A.E. (1995) The aqueous geochemistry of  
417 Zr and the solubility of some Zr-bearing minerals. Applied Geochemistry, 10,  
418 603–620.
- 419 Anczkiewicz, R., Oberli, F., Burg, J., Villa, I., Günther, D., and Meier, M. (2001)  
420 Timing of normal faulting along the Indus Suture in Pakistan Himalaya and a  
421 case of major  $^{231}\text{Pa}/^{235}\text{U}$  initial disequilibrium in zircon. Earth and Planetary  
422 Science Letters, 191, 101–114.
- 423 Ayers, J., Zhang, L., Luo, Y., and Peters, T. (2012) Zircon solubility in alkaline  
424 aqueous fluids at upper crustal conditions. Geochimica et Cosmochimica Acta,  
425 96, 18–28.
- 426 Bau, M. (1996) Controls on the fractionation of isovalent trace elements in magmatic  
427 and aqueous systems: evidence from Y/Ho, Zr/Hf, and lanthanide tetrad effect.  
428 Contributions to Mineralogy and Petrology, 123, 323–333.
- 429 Bau, M., and Dulski, P. (1995) Comparative study of yttrium and rare-earth element  
430 behaviours in fluorine-rich hydrothermal fluids. Contributions to Mineralogy and  
431 Petrology, 119, 213–223.
- 432 Belousova, E., Griffin, W., and O'Reilly, S.Y. (2006) Zircon crystal morphology, trace  
433 element signatures and Hf isotope composition as a tool for petrogenetic  
434 modelling: examples from Eastern Australian granitoids. Journal of Petrology, 47,  
435 329–353.

- 436 Black, L.P., Kamo, S.L., Allen, C.M., Davis, D.W., Aleinikoff, J.N., Valley, J.W.,  
437 Mundil, R., Campbell, I.H., Korsch, R.J., and Williams, I.S. (2004) Improved  
438  $^{206}\text{Pb}/^{238}\text{U}$  microprobe geochronology by the monitoring of a  
439 trace-element-related matrix effect; SHRIMP, ID-TIMS, ELA-ICP-MS and  
440 oxygen isotope documentation for a series of zircon standards. *Chemical*  
441 *Geology*, 205, 115–140.
- 442 Blundy, J., and Wood, B. (1994) Prediction of crystal melt partition coefficients from  
443 elastic moduli. *Nature*, 372, 452–454.
- 444 Breiter, K., Lamarão, C.N., Borges, R.M.K., and Dall'Agnol, R. (2014) Chemical  
445 characteristics of zircon from A-type granites and comparison to zircon of S-type  
446 granites. *Lithos*, 192, 208–225.
- 447 Breiter, K., and Škoda, R. (2012) Vertical zonality of fractionated granite plutons  
448 reflected in zircon chemistry: the Cínovec A-type versus the Beauvoir S-type  
449 suite. *Geologica Carpathica*, 63, 383–398.
- 450 Burakov, B., Hanchar, J., Zamoryanskaya, M., Garbuzov, V., and Zirlin, V. (2002)  
451 Synthesis and investigation of Pu-doped single crystal zircon,  $(\text{Zr,Pu})\text{SiO}_4$ .  
452 *Radiochimica acta*, 90, 95–97.
- 453 Burnham, C.W. (1979) The importance of volatile constituents. In H.S. Yoder, Ed.,  
454 *The evolution of the igneous rocks, fiftieth anniversary perspectives*, p. 439–482.  
455 Princeton University Press, Princeton, New Jersey.
- 456 Caruba, R., Baumer, A., Ganteaume M., and Iacconi, P. (1985) An experimental study  
457 of hydroxyl groups and water in synthetic and natural zircons: a model of the

- 458 metamict state. *American Mineralogist*, 70, 1224–1231.
- 459 Cavosie, A.J., Valley, J.W., and Wilde, S.A. (2006) Correlated microanalysis of zircon:  
460 Trace element,  $\delta^{18}\text{O}$ , and U–Th–Pb isotopic constraints on the igneous origin of  
461 complex > 3900Ma detrital grains. *Geochimica et Cosmochimica Acta*, 70, 5601–  
462 5616.
- 463 Cheng, W.R., Fontan, F., and Monchoux, P. (1992) Mineraux disseminés comme  
464 indicateurs du caractère pegmatitique du granite de Beauvoir, Massif  
465 d'Echassières, Allier, France. *The Canadian Mineralogist*, 30, 763–770.
- 466 Crepaldi, E.L., de AA Soler-Illia, G.J., Grosso, D., and Sanchez, C. (2003)  
467 Nanocrystallised titania and zirconia mesoporous thin films exhibiting enhanced  
468 thermal stability. *New Journal of Chemistry*, 27, 9–13.
- 469 El-Bialy, M.Z., and Ali, K.A. (2013) Zircon trace element geochemical constraints on  
470 the evolution of the Ediacaran (600–614Ma) post-collisional Dokhan Volcanics  
471 and Younger Granites of SE Sinai, NE Arabian–Nubian Shield. *Chemical*  
472 *Geology*, 360, 54–73.
- 473 Eby, G. N., (1990) The A-type granitoids—A review of their occurrence and chemical  
474 characteristics and speculations on their petrogenesis. *Lithos*, 26, 115–134.
- 475 Eby, G. N., 1992, Chemical subdivision of the A-type granitoids—Petrogenetic and  
476 Tectonic Implications. *Geology*, 20, 641–644.
- 477 Erdmann, S., Wodicka, N., Jackson, S., and Corrigan, D. (2013) Zircon textures and  
478 composition: refractory recorders of magmatic volatile evolution? *Contributions*  
479 *to Mineralogy and Petrology*, 165, 45–71.

- 480 Es'kova, E. (1959) Geochemistry of Nb and Ta in the nepheline syenite massifs of the  
481 Vishnevye Mountains. *Geokhimiya*, 2, 130–139.
- 482 Finch, R.J., and Hanchar, J.M. (2003) Structure and chemistry of zircon and  
483 zircon-group minerals. *Reviews in mineralogy and geochemistry*, 53, 1–25.
- 484 Finlow-Bates, T., and Stumpfl, E.F. (1981) The behaviour of so-called immobile  
485 elements in hydrothermally altered rocks associated with volcanogenic  
486 submarine-exhalative ore deposits. *Mineralium Deposita*, 16, 319–328.
- 487 Frost, C.D., and Frost, B.R. (2010) On ferroan (A-type) granitoids: their  
488 compositional variability and modes of origin. *Journal of Petrology*, egg070.
- 489 Geisler, T., Schaltegger, U., and Tomaschek, F. (2007) Re-equilibration of zircon in  
490 aqueous fluids and melts. *Elements*, 3, 43–50.
- 491 Griffin, W., Wang, X., Jackson, S., Pearson, N., O'Reilly, S.Y., Xu, X.X., and Zhou,  
492 X.M. (2002) Zircon chemistry and magma mixing, SE China: in-situ analysis of  
493 Hf isotopes, Tonglu and Pingtan igneous complexes. *Lithos*, 61, 237–269.
- 494 Grimes, C.B., John, B.E., Cheadle, M.J., Mazdab, F.K., Wooden, J.L., Swapp, S., and  
495 Schwartz, J.J. (2009) On the occurrence, trace element geochemistry, and  
496 crystallization history of zircon from in situ ocean lithosphere. *Contributions to  
497 Mineralogy and Petrology*, 158, 757–783.
- 498 Grimes, C.B., John, B.E., Kelemen, P., Mazdab, F., Wooden, J., Cheadle, M.J.,  
499 Hanghøj, K., and Schwartz, J. (2007) Trace element chemistry of zircons from  
500 oceanic crust: a method for distinguishing detrital zircon provenance. *Geology*,  
501 35, 643–646.

- 502 Hanchar, J.M., Finch, R.J., Hoskin, P.W., Watson, E.B., Cherniak, D.J., and Mariano,  
503 A.N. (2001) Rare earth elements in synthetic zircon: Part 1. Synthesis, and rare  
504 earth element and phosphorus doping. *American Mineralogist*, 86, 667–680.
- 505 Hoskin, P.W., and Schaltegger, U. (2003) The composition of zircon and igneous and  
506 metamorphic petrogenesis. *Reviews in mineralogy and geochemistry*, 53, 27–62.
- 507 Kovalenko, V., Tsaryeva, G., Goreglyad, A., Yarmolyuk, V., Troitsky, V., Hervig, R.,  
508 and Farmer, G. (1995) The peralkaline granite-related Khaldzan-Buregtey rare  
509 metal (Zr, Nb, REE) deposit, western Mongolia. *Economic Geology*, 90, 530–  
510 547.
- 511 Li, C.Y., Zhang, H., Wang, F.Y., Liu, J.Q., Sun, Y.L., Hao, X.L., Li, Y.L., and Sun,  
512 W.D. (2012) The formation of the Dabaoshan porphyry molybdenum deposit  
513 induced by slab rollback. *Lithos*, 150, 101–110.
- 514 Nasdala, L., Kronz, A., Wirth, R., Váczi, T., Pérez-Soba, C., Willner, A., and Kennedy,  
515 A.K. (2009) The phenomenon of deficient electron microprobe totals in  
516 radiation-damaged and altered zircon. *Geochimica et Cosmochimica Acta*, 73,  
517 1637–1650.
- 518 Onuma, N., Higuchi, H., Wakita, H., and Nagasawa, H. (1968) Trace element partition  
519 between two pyroxenes and the host lava. *Earth and Planetary Science Letters*, 5,  
520 47–51.
- 521 Pearce, N.J., Perkins, W.T., Westgate, J.A., Gorton, M.P., Jackson, S.E., Neal, C.R.,  
522 and Chenery, S.P. (1997) A compilation of new and published major and trace  
523 element data for NIST SRM 610 and NIST SRM 612 glass reference materials.



- 524 Geostandards newsletter, 21, 115–144.
- 525 Patwe, S.J., Achary, S.N., and Tyagi, A.K. (2009) Lattice thermal expansion of  
526 zircon-type LuPO<sub>4</sub> and LuVO<sub>4</sub>: A comparative study. American Mineralogist,  
527 94(1), 98–104.
- 528 Pupin, J. (1980) Zircon and granite petrology. Contributions to Mineralogy and  
529 Petrology, 73, 207–220.
- 530 Rubin, J.N., Henry, C.D., and Price, J.G. (1993) The mobility of zirconium and other  
531 “immobile” elements during hydrothermal alteration. Chemical Geology, 110,  
532 29–47.
- 533 Robinson, K., Gibbs, G.V., and Ribbe, P.H. (1971) The structure of zircon: a  
534 comparison with garnet. American Mineralogist, 56, 782–790.
- 535 Salvi, S., and Williams-Jones, A.E. (2006) Alteration, HFSE mineralization and  
536 hydrocarbon formation in peralkaline igneous systems: Insights from the Strange  
537 Lake Pluton, Canada. Lithos, 91, 19–34.
- 538 Schaltegger, U. (2007) Hydrothermal zircon. Elements, 3, 51–79.
- 539 Schmitt, A.K., Trumbull, R.B., Dulski, P., and Emmermann, R. (2002) Zr-Nb-REE  
540 mineralization in peralkaline granites from the Amis Complex, Brandberg  
541 (Namibia): evidence for magmatic pre-enrichment from melt inclusions.  
542 Economic Geology, 97, 399–413.
- 543 Sun, S.-S., and McDonough, W. (1989) Chemical and isotopic systematics of oceanic  
544 basalts: implications for mantle composition and processes. Geological Society,  
545 London, Special Publications, 42, 313–345.

- 546 Thomas, R., Webster, J.D., Rhede, D., Serfert, W., Rickers, K., Forster, H.J., Heinrich,  
547 W., and Davidson, P. (2006) The transition from peraluminous to peralkaline  
548 granitic melts: Evidence from melt inclusions and accessory minerals. *Lithos*,  
549 137–149.
- 550 Tu, X.L., Zhang, H., Deng, W.F., Ling, M.X., Liang, H.Y., Liu, Y., and Sun, W.D.  
551 (2011) Application of RESOLUTION in-situ laser ablation ICP-MS in trace element  
552 analyses. *Geochimica*, 40, 83–98 (in Chinese with English abstract).
- 553 Valley, J.W. (2003) Oxygen isotopes in zircon. *Reviews in Mineralogy and*  
554 *Geochemistry*, 53, 343–385.
- 555 Van Lichtervelde, M., Melcher, F., and Wirth, R. (2009) Magmatic vs. hydrothermal  
556 origins for zircon associated with tantalum mineralization in the Tanco pegmatite,  
557 Manitoba, Canada. *American Mineralogist*, 94, 439–450.
- 558 Veksler, I.V., Dorfman, A.M., Kamenetsky, M., Dulski, P., and Dingwell, D.B. (2005)  
559 Partitioning of lanthanides and Y between immiscible silicate and fluoride melts,  
560 fluorite and cryolite and the origin of the lanthanide tetrad effect in igneous rocks.  
561 *Geochimica et Cosmochimica Acta*, 69, 2847–2860.
- 562 Wang, R.C., Fontan, F., Xu, S.J., C, X.M., and Monchoux, P. (1996) Hafnian zircon  
563 from the apical part of the Suzhou granite, China. *The Canadian Mineralogist*, 34,  
564 1001–1010.
- 565 Wu, F.Y., Lin, J.Q., Wilde, S.A., Zhang, X.O., and Yang, J.H. (2005) Nature and  
566 significance of the Early Cretaceous giant igneous event in eastern China. *Earth*  
567 *and Planetary Science Letters*, 233, 103–119.

- 568 Xie, L., Wang, R.C., Chen, X.M., Qiu, J.S., and Wang, D.Z. (2005) Th-rich zircon  
569 from peralkaline A-type granite: Mineralogical features and petrological  
570 implications. *Chinese Science Bulletin*, 50, 809–817.
- 571 Yang, W.B., Niu, H.C., Shan, Q., Sun, W.D., Zhang, H., Li, N.B., Jiang, Y.H., and Yu,  
572 X.Y. (2014) Geochemistry of magmatic and hydrothermal zircon from the highly  
573 evolved Baerzhe alkaline granite: implications for Zr-REE-Nb mineralization.  
574 *Mineralium Deposita*, 49, 451–470.
- 575 Yang, W.B., Niu, H.C., Sun, W.D., Shan, Q., Zheng, Y.F., Li, N.B., Li, C.Y., Arndt,  
576 N.T., Xu, X., Jiang, Y.H., and Yu, X.Y. (2013) Isotopic evidence for continental  
577 ice sheet in mid-latitude region in the supergreenhouse Early Cretaceous.  
578 *Scientific reports*, 3: 2732, DOI: 10.1038/srep02732.
- 579 Yang, J.H., Wu, F.Y., Wilde, S.A., Chen, F., Liu, X.M., and Xie, L.W. (2008)  
580 Petrogenesis of an alkali syenite–granite–rhyolite suite in the Yanshan Fold and  
581 Thrust Belt, Eastern North China Craton: geochronological, geochemical and  
582 Nd–Sr–Hf isotopic evidence for lithospheric thinning. *Journal of Petrology*,  
583 49(2), 315–351.
- 584 Yin, R., Wang, R.C., Zhang, A.C., Hu, H., Zhu, J.C., Rao, C., and Zhang, H. (2013)  
585 Extreme fractionation from zircon to hafnon in the Koktokay No. 1 granitic  
586 pegmatite, Altai, northwestern China. *American Mineralogist*, 98, 1714–1724.
- 587 Zheng, Y.F., Wu, Y.B., Gong, B., Chen, R.X., Tang, J., and Zhao, Z.F. (2007) Tectonic  
588 driving of Neoproterozoic glaciations: Evidence from extreme oxygen isotope  
589 signature of meteoric water in granite. *Earth and Planetary Science Letters*, 256,

590 196–210.

591

592

593 **Figure captions**

594 **FIGURE 1.** (a) Simplified geological map of eastern China, showing major tectonic  
595 units (modified after Wu et al. 2005). (b) Simplified geological map of the Cretaceous  
596 Xiangshan complex, where the arfvedsonite granites are surrounded by biotite  
597 granites.

598

599 **FIGURE 2.** (a)  $(Zr+Nb+Ce+Y)$  vs  $(Na_2O+K_2O)/CaO$  diagram, showing the  
600 Xiangshan arfvedsonite granites are of A-type affinity. (b)  $Y/Nb$  vs  $Yb/Ta$  diagram for  
601 the Xiangshan arfvedsonite granites (according to Eby, 1992). Composition data are  
602 listed in Supplemental Data Table 1. OIB=oceanic island basalt; IAB=island arc basalt.  
603 Fields with dashed lines represent A<sub>1</sub>- and A<sub>2</sub>-type granites of Eby (1990).

604

605 **FIGURE 3.** Plan-polarized microphotographs, CL and BSE images of zircons from  
606 the Xiangshan arfvedsonite granites. (a) Microphotograph of interstitial Type-1A  
607 zircon between quartz and arfvedsonite. (b) Microphotograph of interstitial Type-1B  
608 zircon between quartz and K-feldspar. (c) Microphotograph of Type-2 zircon enclosed  
609 in graphic texture. (d) CL image of Type-1A zircon with oscillatory zoning. (e) CL  
610 image of Type-1B zircon with pores and inclusions, and with no oscillatory growth  
611 zones. (f) CL image of Type-2 zircon with slight oscillatory growth zones. (g) BSE  
612 image of Type-1A zircon with melt inclusions. (h) BSE image of Type-1B zircon with  
613 thorite and Fe-oxide. (i) Microphotograph of Type-2 zircon coexisted with fluid  
614 inclusions.

615

616 **FIGURE 4.** Type-1B zircon occurs as overgrowth on Type-1A zircon. (a) CL image.  
617 (b) BSE image. (c) Full-widths at half-maximum (FWHM) mapping by Raman  
618 spectrum. (d–i) Element mapping by EMPA show the distribution of Th, U, Hf, Y, P  
619 and Fe, respectively.

620

621 **FIGURE 5.** XRD patterns adopted in situ on single zircon crystals from the  
622 Xiangshan arfvedsonite granites, compared with the standard zircon (06-0266).

623

624 **FIGURE 6.** (a) Chondrite-normalized REE diagram for zircons from the Xiangshan  
625 arfvedsonite granites. (b) Primitive Mantle normalized trace elements diagram for  
626 zircons from the Xiangshan arfvedsonite granites. Chondrite and PM data are from  
627 Sun and McDonough (1989).

628

629 **FIGURE 7.** Variation diagrams of trace element contents for zircon from the  
630 Xiangshan pluton. (a) Zr+Hf (apfu) vs. Si (apfu) diagram, the dashed line show ideal  
631 occupation (Zr+Hf)/Si=1 (b) Hf (apfu) vs. Zr (apfu) diagram, apfu means atoms per  
632 formula units. (c) Th (ppm) vs. U (ppm) diagram. (d) REE+Y (mole) vs. P (mole)  
633 diagram, cation contents were calculated on the basis of one mole zircon.

634

635 **FIGURE 8.** Variation diagrams of SiO<sub>2</sub> vs. 1-Total contents, showing the increasing  
636 trace elements and volatiles contents of zircons from early- to late-granitic system.

637 The relative deviations of SiO<sub>2</sub> contents from 32.8 wt% are indicative of volatile  
638 contents.

639

640 **FIGURE 9.** Zircon-melt trace element partition coefficients as a function of ionic  
641 radius, showing the increasing of trace elements partitioning from early- to late-stage  
642 zircon. Data is taken from the average values of Type-1A zircon (a), Type-1B zircon  
643 (b), and Type-2 zircon (c) to whole-rock compositions (Table 2). The REE curves is  
644 showing least-squares fits of the Blundy and Wood (1994) theoretical structural strain  
645 model to the data.

646

647 **FIGURE 10.** A schematic drawing illustrates the formation of the three zircon types  
648 during the magmatic-hydrothermal evolution of the Xiangshan arfvedsonite granites.  
649 The temperature of solvus was assumed at ca. 725 °C at 100 Mpa. The critical point  
650 of the evolution curve of granitic melt with H<sub>2</sub>O contents is referred from Thomas et  
651 al. (2006). The inset show morphological types of zircon observed in the Xiangshan  
652 arfvedsonite granites, according to Pupin (1980).

653

654 Table 1 Cell parameters of three types of zircon determined by XRD, compared with  
 655 standard zircon (06-0266).

Zircon types	a	c	V	c/a	Two theta (at ca. 27°)
Type-1A	6.603(2)	5.971(4)	260.3	0.904	26.94
Type-1B	6.649(6)	6.020(2)	266.1	0.905	26.82
Type-2	6.677(7)	6.010(4)	267.9	0.900	26.65
Zircon (06-0266)	6.607	5.982	261.1	0.905	26.98

656 Notes: unit-cell parameters (a,c) in Å; unit-cell volume in Å<sup>3</sup>.

657

658

659 Table 2 Trace element partition coefficients of the three types of zircon to host melt  
 660 (whole-rock composition) and the ionic radii.

Elements	Type-1A/Melt	Type-1B/Melt	Type-2/Melt	Ionic radii (Å)
P <sup>5+</sup>	2.65	21.6	51.4	0.520
Ti <sup>4+</sup>	0.005	0.046	1.50	0.745
Y <sup>3+</sup>	56.7	317	777	1.040
Nb <sup>5+</sup>	0.48	19.2	15.7	0.780
La <sup>3+</sup>	0.02	0.54	0.02	1.172
Ce <sup>3+</sup>	0.34	2.36	5.24	1.150
Pr <sup>3+</sup>	0.03	0.82	0.79	1.130
Nd <sup>3+</sup>	0.11	1.25	3.90	1.123
Sm <sup>3+</sup>	1.06	5.16	50.3	1.098
Eu <sup>3+</sup>	0.55	3.43	9.16	1.087
Gd <sup>3+</sup>	7.62	26.1	252	1.078
Tb <sup>3+</sup>	14.9	60.4	417	1.063
Dy <sup>3+</sup>	29.0	129	602	1.052
Ho <sup>3+</sup>	52.6	253	771	1.041
Er <sup>3+</sup>	77.8	423	852	1.030
Tm <sup>3+</sup>	101	622	894	1.020
Yb <sup>3+</sup>	133	895	913	1.008
Lu <sup>3+</sup>	150	968	748	1.001
Hf <sup>4+</sup>	874	1534	1578	0.850
Ta <sup>5+</sup>	3.12	95.7	78.8	0.780
Th <sup>4+</sup>	12.5	664	551	1.080
U <sup>4+</sup>	109	2321	472	1.030

661



# Figure 1

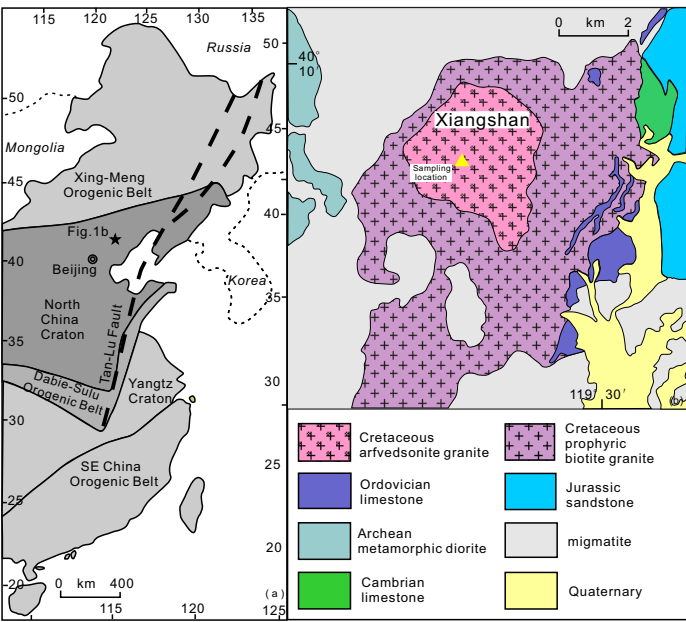


# Figure 2

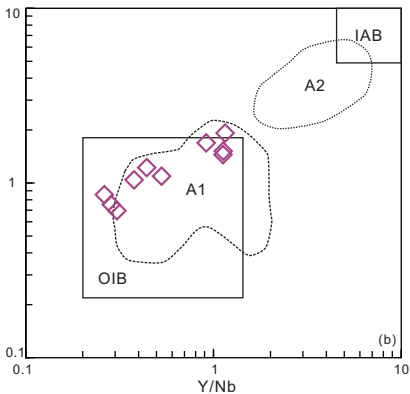
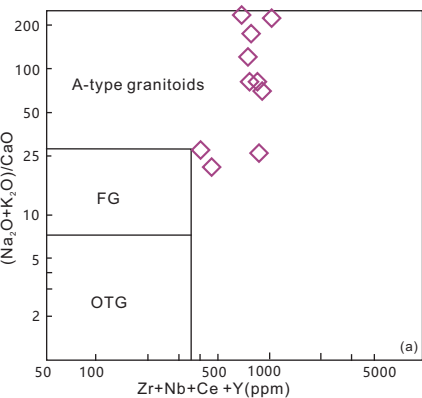


# Figure 3

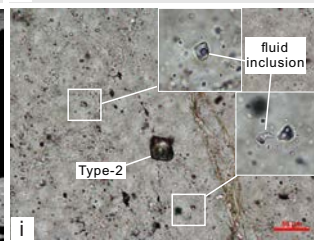
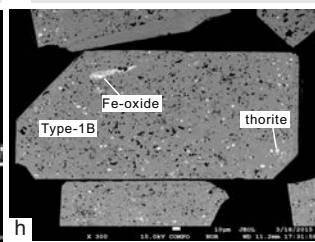
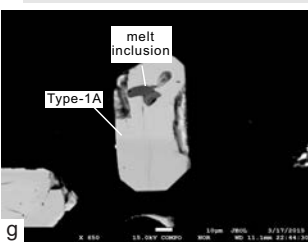
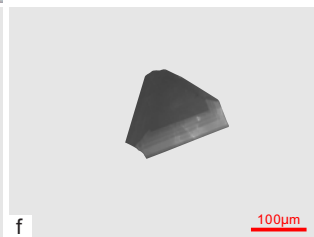
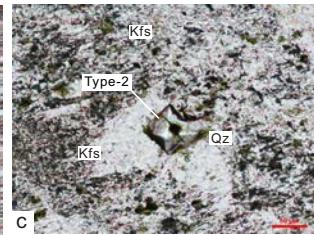
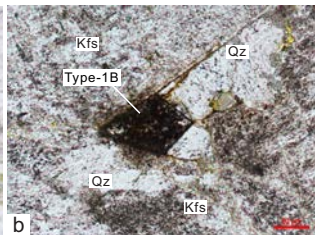
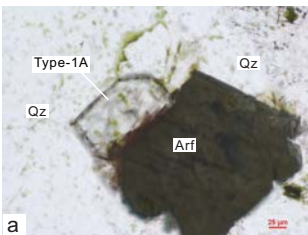


Figure 4

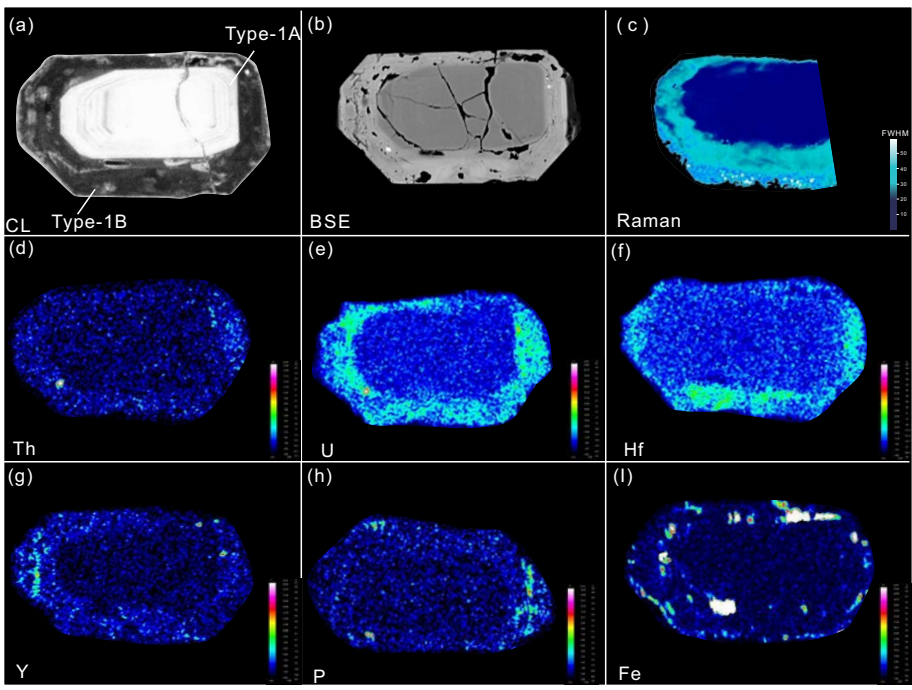
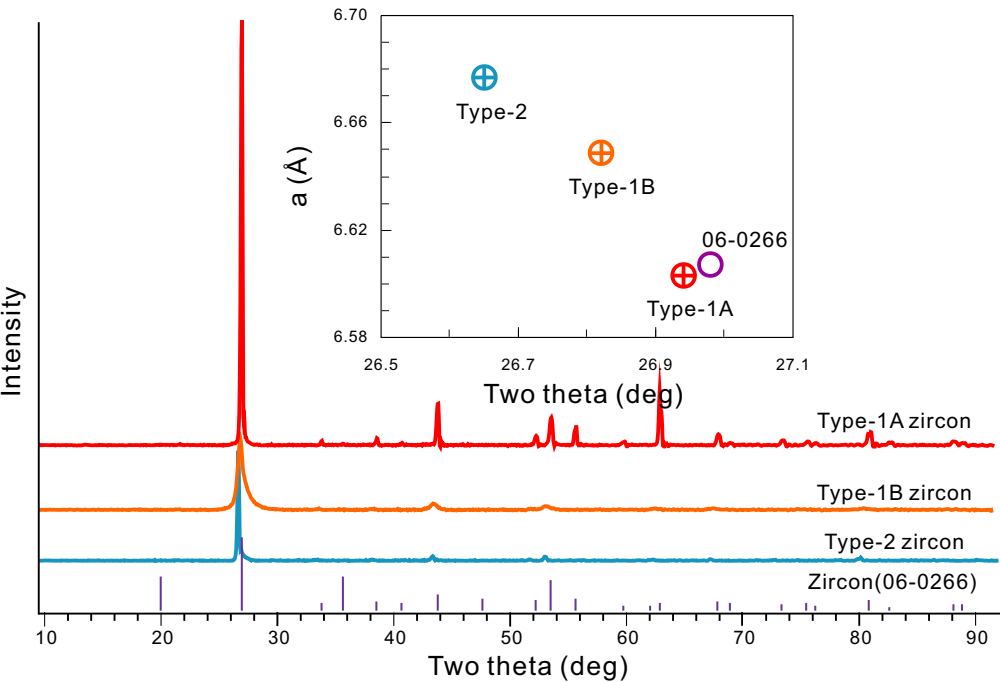
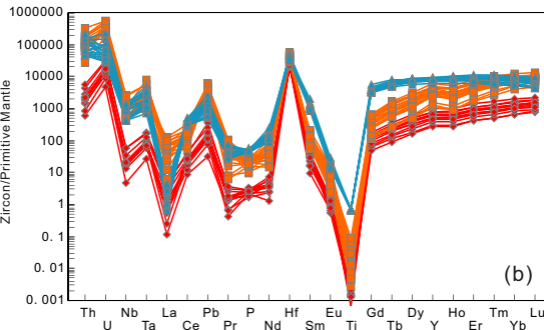
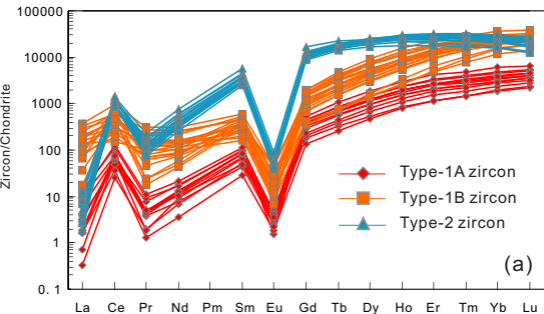


Figure 5



# Figure 6



# Figure 7

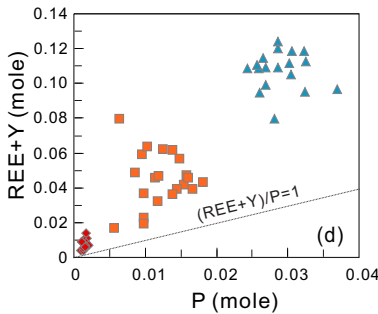
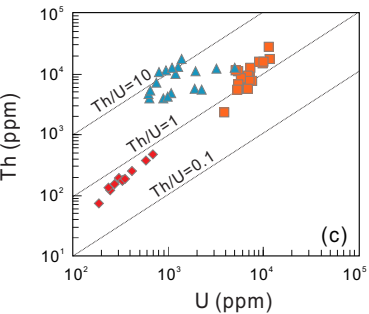
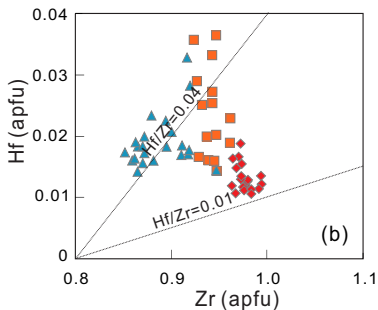
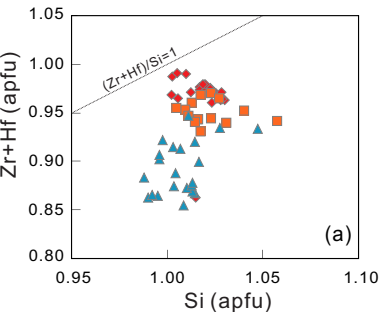






# Figure 9

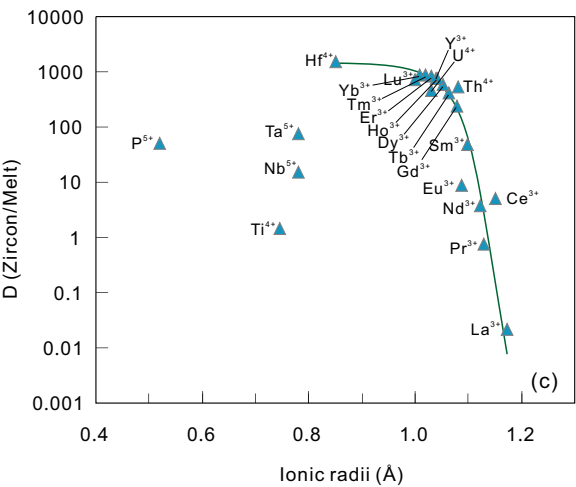
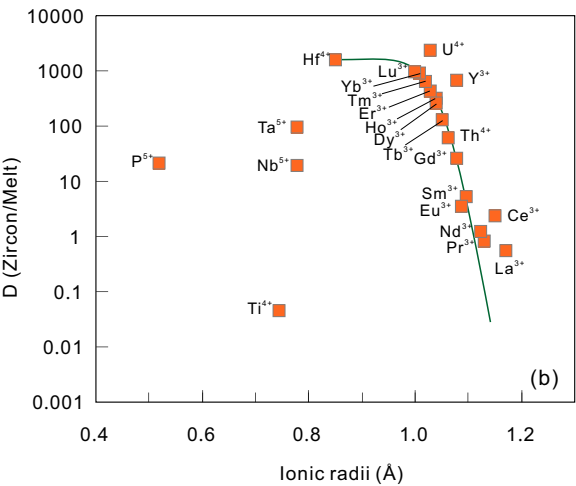
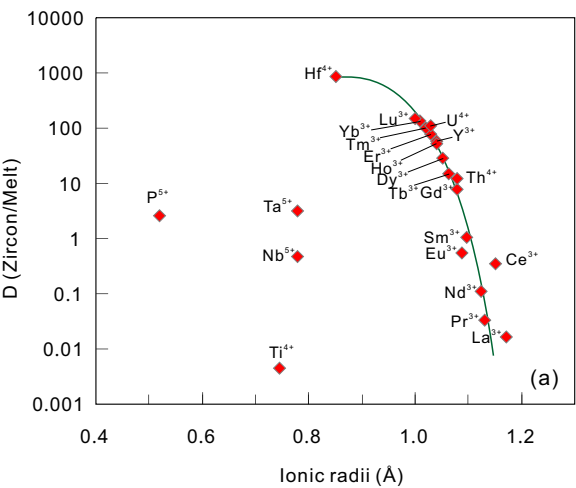


# Figure 10

